# REPORT DOCUMENTATION PAGE

Form Approved OMB NO. 0704-0188



| 1. REPORT DATE (DD-MM-YYYY) | 2. REPORT TYPE | 3. DATES COVERED (From - To) |
|---|---|---|
| 21-09-2015 | MS Thesis | - |

4. TITLE AND SUBTITLE
Exfoliation and Air Stability of Germanane

5a. CONTRACT NUMBER
W911NF-12-1-0481

5b. GRANT NUMBER

5c. PROGRAM ELEMENT NUMBER
611102

6. AUTHORS
Sheneve Butler

5d. PROJECT NUMBER

5e. TASK NUMBER

5f. WORK UNIT NUMBER

7. PERFORMING ORGANIZATION NAMES AND ADDRESSES
Ohio State University
1960 Kenny Road

Columbus, OH 43210 -1016

8. PERFORMING ORGANIZATION REPORT NUMBER

9. SPONSORING/MONITORING AGENCY NAME(S) AND ADDRESS (ES)
U.S. Army Research Office
P.O. Box 12211
Research Triangle Park, NC 27709-2211

10. SPONSOR/MONITOR'S ACRONYM(S)
ARO

11. SPONSOR/MONITOR'S REPORT NUMBER(S)
62249-MS.12

12. DISTRIBUTION AVAILIBILITY STATEMENT
Approved for public release; distribution is unlimited.

13. SUPPLEMENTARY NOTES
The views, opinions and/or findings contained in this report are those of the author(s) and should not contrued as an official Department of the Army position, policy or decision, unless so designated by other documentation.

14. ABSTRACT
Exfoliation of graphene has shown that it is not only possible to create stable, singleatom- thick sheets from a crystalline solid, but that these materials have fundamentally different properties than the parent material. Modifying the surface of graphene has been challenging because of its sp2 hybridization. Within the same family of carbon there are the possibilities of layered materials that are structurally similar to graphene, however, contains the sp3 hybridization needed for functionalization. This functionalization could lead to a tunable band gap necessary for optoelectronics.

15. SUBJECT TERMS
2D Materials beyond graphene, Germanane

| 16. SECURITY CLASSIFICATION OF: | | | 17. LIMITATION OF ABSTRACT | 15. NUMBER OF PAGES | 19a. NAME OF RESPONSIBLE PERSON |
|---|---|---|---|---|---|
| a. REPORT | b. ABSTRACT | c. THIS PAGE | | | Joshua Goldberger |
| UU | UU | UU | UU | | 19b. TELEPHONE NUMBER 614-247-7438 |

**Report Title**

Exfoliation and Air Stability of Germanane


**ABSTRACT**

Exfoliation of graphene has shown that it is not only possible to create stable, singleatom- thick sheets from a crystalline solid, but that these materials have fundamentally different properties than the parent material. Modifying the surface of graphene has been challenging because of its sp2 hybridization. Within the same family of carbon there are the possibilities of layered materials that are structurally similar to graphene, however, contains the sp3 hybridization needed for functionalization. This functionalization could lead to a tunable band gap necessary for optoelectronics.

Germanane, an sp3 derivative of graphene, can be mechanically exfoliated as single and few layers onto SiO2/Si substrates. Exfoliation was achieved by mechanical exfoliation using molds of PDMS. Detection of the few and single layers were achieved via optical microscopy on 100 nm thick SiO2/Si substrates. To obtain an accurate height profile for the sheets, atomic force microscopy (AFM) was used after calibration of the tip to sample/substrate interaction.

For use in optoelectronic and sensing applications, air stability of germanane must be probed. Attenuated total reflection Fourier transform infrared (ATR-FTIR) spectroscopy was used to detect changes at the germanane surface by monitoring the Ge—H stretching mode. There was no change observed over 60 days meaning that the germanane surface remains intact. Another technique used to probe the surface was X-ray Photoelectron Spectroscopy (XPS). XPS spectra showed that the surface layer slowly oxidizes in air over the span of 5 months, while the underlying layers are resilient to oxidation based on etching 0.5 nm of surface.

# Exfoliation and Air Stability of Germanane

Thesis

Presented in Partial Fulfillment of the Requirements for the Degree Master of Science in the Graduate School of The Ohio State University

By

Sheneve Z. Butler

Graduate Program in Chemistry

The Ohio State University

2013

Master's Examination Committee:

Joshua E. Goldberger, Advisor

Terry Gustafson, Advisor

## Abstract

Exfoliation of graphene has shown that it is not only possible to create stable, single-atom-thick sheets from a crystalline solid, but that these materials have fundamentally different properties than the parent material. Modifying the surface of graphene has been challenging because of its $sp^2$ hybridization. Within the same family of carbon there are the possibilities of layered materials that are structurally similar to graphene, however, contains the $sp^3$ hybridization needed for functionalization. This functionalization could lead to a tunable band gap necessary for optoelectronics.

Germanane, an $sp^3$ derivative of graphene, can be mechanically exfoliated as single and few layers onto $SiO_2$/Si substrates. Exfoliation was achieved by mechanical exfoliation using molds of PDMS. Detection of the few and single layers were achieved via optical microscopy on 100 nm thick $SiO_2$/Si substrates. To obtain an accurate height profile for the sheets, atomic force microscopy (AFM) was used after calibration of the tip to sample/substrate interaction.

For use in optoelectronic and sensing applications, air stability of germanane must be probed. Attenuated total reflection Fourier transform infrared (ATR-FTIR) spectroscopy was used to detect changes at the germanane surface by monitoring the Ge—H stretching mode. There was no change observed over 60 days meaning that the germanane surface remains intact. Another technique used to probe the surface was X-ray Photoelectron Spectroscopy (XPS). XPS spectra showed that the surface layer slowly oxidizes in air

over the span of 5 months, while the underlying layers are resilient to oxidation based on etching 0.5 nm of surface.

Dedication

This document is dedicated to my family.

# Acknowledgments

The Acknowledgments page is optional. This page includes a brief, sincere, professional acknowledgment of the assistance received from individuals, advisor, faculty, and institution.

## Vita

May 2006 .....Lithia Springs High School

2010.....B.A. Chemistry, Agnes Scott College

2010 to present .....Graduate Teaching Associate, Department of Chemistry, The Ohio State University

## Publications

Bianco, E., Butler, S., Jiang, S., Restrepo, O., Windl, W., and Goldberger J. *Stability and Exfoliation of Germanane: A Germanium Graphane Analogue*, ACS Nano **Article ASAP**

Butler, S.Z., Hollen, S.M., Cao, L., Cui, Y., Gupta, J.A., Gutiérrez, H.R., Heinz, T.F., Hong, S.S., Huang, J, Ismach, A.F., *et al.* Progress, Challenges, and Opportunities in Two-Dimensional Materials Beyond Graphene, ACS Nano, **Article ASAP**

## Fields of Study

Major Field: Chemistry

Table of Contents

List of Tables

List of Figures

# Chapter 1: Introduction

Nanoscience and nanotechnology have arisen as pillars of scientific research that will lead us to the next industrial revolution and map the course of scientific and technological advancements in the 21st century. Progress has been due to the development of sophisticated theoretical and experimental techniques, practical tools, for understanding characterizing and manipulating nanoscale structures, processes and systems. The fundamental entities of interest to nanoscience and nanotechnology are the isolated structures and their assemblies. Structures in the nanoscale are considered at the borderline of the smallest of human made devices and the largest molecules of living systems. Nanostructures are the building blocks of nanotechnology, and the formation of their assemblies requires a deep understanding of the interactions between individual atoms and molecules forming the nanostructures. The science of the ultrasmall is leading to new paradigms on the basic properties of materials; it is also expected to lead to the fabrication of novel high-technological devices in many fields of application from electronics to medicine. Increase the level of technological advance at a significantly higher rate than ever experienced in human history.

In addition to the rise of new technologies, a novel class of low dimensional systems distinguishes the development of nanoscale sciences. For example, the zero-dimensional class of quantum dots,[1-3] one-dimensional class of nanoribbons, nanotubes, and nanowires,[4,5] and two-dimensional (2D) class of graphene and single-atomically thin

materials.[6] Each class comes with its own set of unexplored physical, chemical, and mechanical properties that aid in understanding their fundamental behavior on the nanoscale. The main focus of the work presented in this thesis will be within this class of 2D materials.

## Two-Dimensional Materials

Two-dimensional materials have been one of the most extensively studied classes of materials due to the vast unusual physical phenomena that occur when charge and heat transport is confined to a plane. 2D sheets with finite-size and quantum characteristics in their electronic and optical properties can be made both uniform and reproducible in size and thickness by many methods currently used in conventional material synthesis. Some remarkable changes occur in the electronic properties of layered materials as their thickness is reduced down to single or only a few layers. Many materials with properties dominated by their two-dimensional structural units include the layered metal dichalcogenides, copper oxides and iron pnictides which exhibit correlated electronic phenomena such as charge density waves and high temperature superconductivity.[7-9] The most well known 2D layered material is the single layer of graphite termed graphene.

### *Graphene*

Graphene, a single atom thick layer consisting of $sp^2$ carbon bonds, was first discovered in the 1960s when researchers observed higher basal plane conductivity in intercalated graphite.[10-12] For the next 40 years, research on graphite continued with hopes of

observing improved electrical properties in thin graphene layers. It was not until 2004 that the exfoliation of single-layer graphene was achieved.[6] Geim and Novoselov used a mechanical method to isolate graphene by peeling bulk graphite on adhesive tape until a thin layer was present, and then transferring it to a substrate. These graphene crystals exhibited unique and fascinating electronic properties like high carrier mobility with ballistic transport (~10, 000 $cm^2V^{-1}s^{-1}$) and half integer quantum Hall effect at room temperature. (26)

Upon further testing, it was shown that graphene has room temperature mobilities of 200,000 $cm^2V^{-1}s^{-1}$.[13,14] Other properties include high thermal conductivity (5000 $Wm^{-1}K^{-1}$),[15] high Young's modulus (~1.0 T Pa)[16] and impermeability (26). Even at one-atom thick, graphene is a fantastic electronic and thermal conductor, and graphene-based materials have been proposed for a host of applications including high-frequency oscillators,[17] field effect transistors,[6,18-22] solar energy processing panels,[3,23-25] transparent conductors,[26,27] and barristor transistor-like devices.[28] Potential advanced material applications include mechanically robust and light-weight material applications including hydrogen visualization templates for TEM, components of satellites and aircraft technology. [29] Furthermore, as single-layer graphene is entirely surface area, its properties and reactivity depend on the substrate, its local electronic environment, and mechanical deformations.

*Two-Dimensional Materials Beyond Graphene*

The experimental isolation of graphene has opened up the possibility of extracting and isolating 2D forms of crystals composed of elements other than carbon. The intense research efforts used to investigate graphene layers can be applied to other layered materials. The past eight years of graphene research has yielded many methods for synthesizing, transferring, detecting, characterizing and manipulating the properties of layered van der Waals materials. Furthermore, novel synthetic methods including topotactic, solution based, solvothermal, and UHV surface epitaxial approaches have unleashed the potential to create new van der Waals solids and single-layer thick materials. These established methods have enabled the field of 2D materials beyond graphene to mature very quickly.

There exists an entire periodic table of crystalline solid-state materials each having different electronic, mechanical, and transport properties, and the possibility to create single-atom or few-atom polyhedral thick 2D layers from any material remains. A natural extension of the study of graphene would be to synthesize graphene analogues of other layered inorganic materials ($WS_2$, $MoS_2$, BN). These materials possess graphite-like layered structures in which the layers are held together by weak van der Waals forces. Since the 1960's, few-layer van der Waals materials have been prepared and studied using the "Scotch tape" mechanical exfoliation method.[30-32] $MoS_2$ and $WS_2$ are pseudo two-dimensional compounds in which the atoms in the layer are bound by strong covalent forces, while van der Waals forces hold the layers together. These layered transition metal dichalcogenides are characteristic of having indirect to direct band gap transitions dependent on the number of layers. $MoS_2$ has an indirect band gap at 1.29 eV,

whereas isolated single layers of $MoS_2$ have a direct gap (1.8 ev).[33] $WS_2$ has indirect band gap at 1.3 eV and a direct gap at 2.1 eV when isolated as a single sheet.[34] Single layers of $MoS_2$ have also attracted much interest as high mobility transistors.[22,33,35]

Another layered material that is isostructurally similar to graphene is hexagonal boron nitride. Sheets of hexagonal-BN are comprised of alternating boron and nitrogen atoms in a honeycomb arrangement consisting of $sp^2$ bonded 2D layers. Hexagonal-BN offers a superior set of properties to graphene such as large band gap (5.9 eV),[36] high optical-transparency,[37] tunable photoluminescence,[38] high mechanical strength,[39] high thermal conductivity,[40,41] and ultraviolet cathodoluminescence.[42]

Many novel materials that had been initially considered to exist only in the realm of theory have been synthesized. These include Group IV and II-VI semiconductors analogues of graphene/graphane (the $sp^2$/H-terminated $sp^3$ derivatives) such as silicene[43-46] and germanane.[47] Similar to graphene, the properties at the single layer are also distinct from the bulk. Furthermore, these 2D materials are useful building blocks that can be restacked and integrated into composites for a wide range of applications. The class of 2D materials of particular interest is a class of 2D materials in the Group IV (or carbon) family called germanane.

Germanane (GeH) is an analogue of graphane, the $sp^3$ derivative of graphene. It consists of a puckered chair structure consisting of H-termination at every Ge atom (**Figure 2.1b**). Previous research has shown that layered Zintl phases such as $CaSi_2$ and $CaGe_2$ can be topochemically deintercalated in aqueous HCl at low temperatures to produce hydrogen-terminated, silicon and germanium van der Waals solids. [48-50] The resulting four-

coordinated puckered lattice of Si and Ge atoms is analogous to that of $sp^3$-hybridized graphane. The silicon lattice oxidizes readily, initially forming siloxene ($SiH_{0.5}(OH)_{0.5}$) sheets that are terminated with either Si-H or Si-OH bonds at the fourth coordination site, which is not amenable to functionalization, and eventually degrades to form $SiO_2$ in ambient conditions.[50,51] These Group IV graphane analogues[52-55] are a particularly intriguing class of systems due to the possibility of utilizing covalent chemistry to modulate and tune the properties.

The main focus of this thesis is the exfoliation and characterization of GeH. Details on the instrumentation as well as on the calibration of thickness of the single layer GeH and air stability of bulk GeH will be discussed.

# Chapter 2: Exfoliation and Detection

## Overview

This chapter investigates a mechanical method to exfoliate single layer GeH from bulk three dimensional flakes. Exfoliation via other methods has proven to be a challenge, and requires further study. Current exfoliation using PDMS has produced small sheets (2 -3 μm) at low yields. Single layer detection of these sheets can be achieved under an optical microscope using 100 nm $SiO_2$/Si substrates.

## Introduction

The reliable synthesis of single and few-layer 2D materials is an essential first step to characterizing the layer-dependent changes in their properties, as well as providing pathways for their integration into a multitude of applications. Meticulous care must be taken to produce pure 2D material of the highest quality meaning the material used for exfoliation contains no impurities and has smooth flat surfaces. After exfoliation, single to few layers must be detectable. Detection is the primary challenge in characterization, which will be addressed in this chapter.

## Exfoliation and Detection

The first challenge in single layer characterization is single layer preparation. Probing the molecular structure of 2D materials is inherently challenging due to the small sample size. However, numerous methods have been developed to enable their identification and characterization. The most common approaches for obtaining single and few-layer thick 2D materials from many of these solids include mechanical exfoliation of large crystals using tape, chemical exfoliation by dispersing in a solvent having the appropriate surface tension, and molecule/atom intercalation in order to exfoliate these layers and enable their dispersion in polar solvents. Mechanical exfoliation is the approach used for transferring GeH to a substrate.

GeH is a part of a common class of crystalline structures called van der Waals solids. These solids can be exfoliated as stable single layers since their crystal structures feature neutral, single-atom-thick or polyhedral-thick layers of atoms that are covalently or ionically bonded with their neighbors within each layer, while the layers are held together via van der Waals bonding along the third axis. The weak interlayer van der Waals energies (~40-70 meV) enable the facile exfoliation of these layers. The isolation of individual and few-layers using mechanical exfoliation remains the most powerful approach for studying their properties since it is considerably less destructive than the other methods, and has successfully been used to create large, 10 μm-sized flakes ranging in thickness from single to few layers.

GeH has been exfoliated using polydimethylsiloxane (PDMS), a silicon based polymer. For exfoliation, PDMS (Sylgard 184) is mixed with a cross-linking agent in a 10:1 ratio and poured into a microstructured mold and heated to 60 $^{o}$C to obtain a replica of the

elastomer mold (PDMS cross-linked). Curing occurs following mixing of PDMS and cross-linking agent, and is evidenced by a gradual increase in viscosity. After "cross-linking", PDMS becomes a flexible elastomer. Pressing two molds of PDMS together (**Figure 2.1c**) and slowly pulling them apart until GeH flakes exfoliate and a thin region is left on the PDMS mold (**Figure 2.1d**). The exfoliated GeH is then transferred to a dielectric coated $SiO_2$/Si substrate for detection (**Figure 2.1e**).

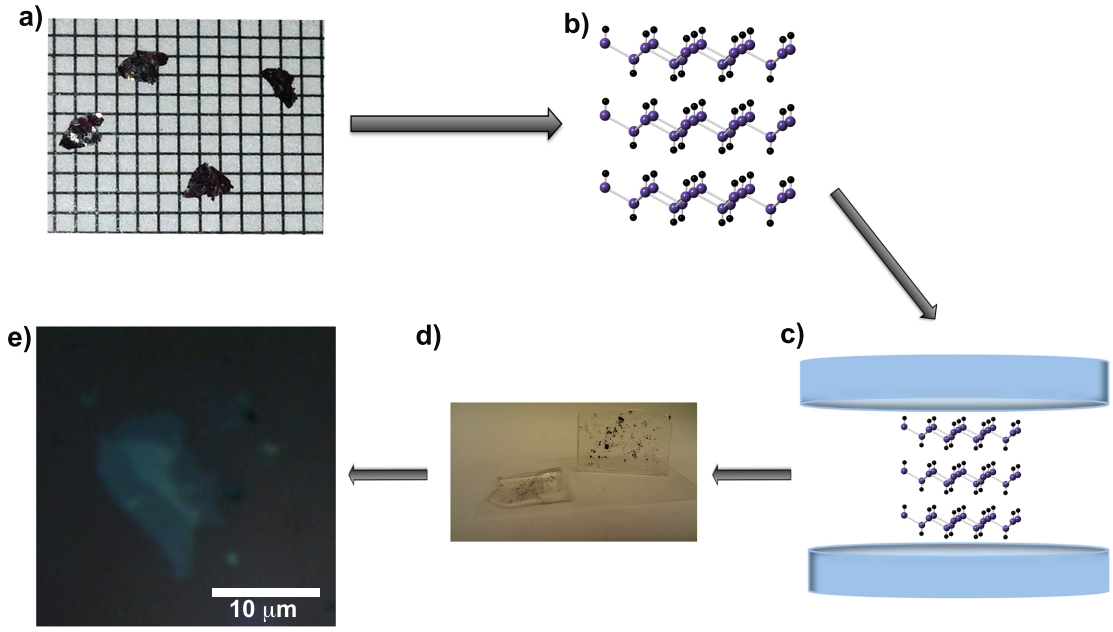


**Figure 2.1** Schematic of exfoliation process for GeH. a) GeH crystals b) Stacked GeH layers c) Stacked GeH between PDMS d) Image of exfoliated GeH on PDMS e) Optical image of exfoliated GeH

The second challenge in single layer characterization is single layer detection. Optical microscopy is still the most powerful high-throughput method for initially identifying

single and multiple-layer flakes.[56-59] Dielectric-coated $SiO_2$/Si substrates are the most common substrates used to visualize and locate single and few layers. The color of the dielectric coated wafer depends on an interference effect from reflection off of the two surfaces of the dielectric. Single and few layer flakes on the surface of the dielectric modify the interference and create a color contrast between the flake and the substrate.[58,60] **Figure 2.2** shows a thin film (in this case a 2D flake) on top of a $SiO_2$ thin film on top of a Si wafer. The contrast between the flake and $SiO_2$ substrate is due to a phase shift of the interference color and material opacity.

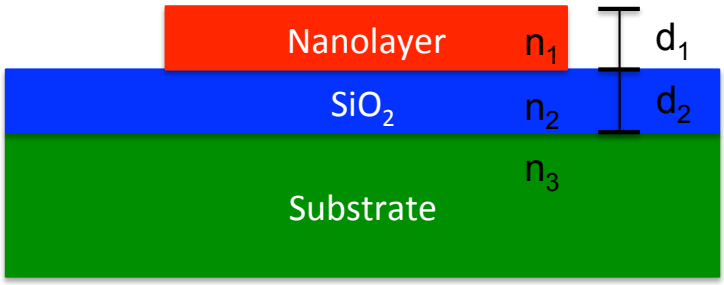


**Figure 2.2** Schematic depiction of nanolayer with thickness $d_1$ and index refraction of $n_1$ deposited on a $SiO_2$ layer with thickness $d_2$ and index of refraction $n_1$ on a Si substrate.

The dependence of the contrast on $SiO_2$ thickness can be explained using Fresnel law. For normal light incidence, the intensity of reflected light from the stacking of two thin films on top of a semi-infinite layer (the Si substrate) is given by[58,60]

$$R(n_1) = \left| \frac{r_1 e^{i(\emptyset_1+\emptyset_2)} + r_2 e^{-i(\emptyset_1-\emptyset_2)} + r_3 e^{-i(\emptyset_1+\emptyset_2)} + r_1 r_2 r_3 e^{i(\emptyset_1-\emptyset_2)}}{e^{i(\emptyset_1-\emptyset_2)} + r_1 r_2 e^{-i(\emptyset_1-\emptyset_2)} + r_1 r_3 e^{-i(\emptyset_1+\emptyset_2)} + r_2 r_3 e^{i(\emptyset_1-\emptyset_2)}} \right|^2 \quad \text{Equation 1}$$

where

$$r_1 = \frac{n_0 - n_1}{n_0 + n_1}, \qquad r_2 = \frac{n_1 - n_2}{n_1 + n_2}, \qquad r_3 = \frac{n_2 - n_3}{n_2 + n_3} \qquad \text{Equation 2}$$

are the relative indices of refraction and $\emptyset_i = \frac{2\pi d_i n_i}{\lambda}$ are the phase shifts induced by changes in the optical path.

The reflected light intensity in the absence of sample can be found by substituting $n_1 = 1$ (refractive index for air):

$$R(n_1 = 1) = \left| \frac{r_2' e^{i(\emptyset_2)} + r_3 e^{-i(\emptyset_2)}}{e^{i(\emptyset_2)} + r_2' r_3 e^{-i(\emptyset_2)}} \right|^2 \qquad \text{Equation 3}$$

where $r_2' = \frac{n_0 - n_2}{n_0 + n_2}$ is the relative index of refraction at the interface between air and the dielectric thin film.

The contrast is defined as the relative intensity of reflected light in the presence and absence of sample and can be written as

$$Contrast = \frac{R(n_1 = 1) - R(n_1)}{R(n_1 = 1)} \qquad \text{Equation 4}$$

In order to determine optimal conditions for optical detection of sample calculated contrast is plot as a function of incident light wavelength and $SiO_2$ thickness. [58,60] The theory slightly overestimates the contrast, attributed to deviations from normal light incidence (because of high NA) and an extinction coefficient of the sample that is unknown. For optimal contrast, the thickness of the dielectric coating needs to be within 5 nm of the ideal value. However, since the index of refraction of many novel materials is unknown, it is often necessary to first experimentally exfoliate onto a range of substrates having different dielectric thicknesses to initially determine the optimal thickness.

Atomic Force Microscopy

Information on surfaces has been provided by the development of scanning probe microscopy (SPM). These techniques developed because of the increasing need to understand and probe physical/chemical features of samples on the atomic scale. SPM evolved primarily as a qualitative imaging method, however, advances in the past decade has widen SPM capabilities to probing electrical, mechanical, optical, and magnetic properties of materials at their fundamental length scales.[61]

Atomic force microscopy (AFM) was invented in 1986 to detect atomic scale features on insulating surfaces under ambient and liquid conditions. AFM uses a sharp tip mounted at the end of a cantilever, which bends in response to the force exerted on the tip by the sample. As the tip interacts with the surface, the attractive and repulsive forces between the cantilever and tip and the surface varies, producing deflections in the cantilever. These deflections are measured, and used to compile a topographic image of the surface.

**Figure 2.3** depicts the forces interacting with the tip as it approaches the surface of the sample.

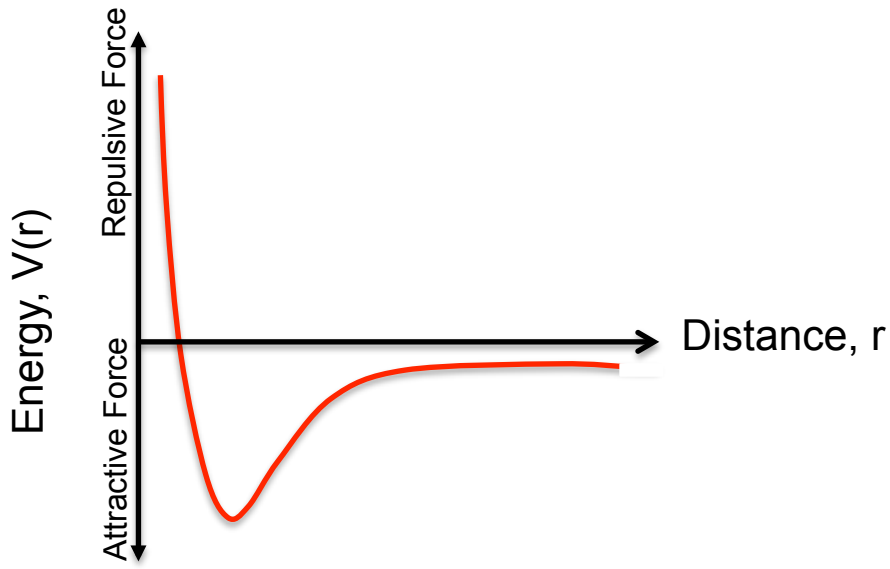


**Figure 2.3** Potential energy curve describing the interactions occuring as the AFM probe is brought close to the sample's surface

The measurement of the forces between atoms and molecules can tell us about their structures and the nature of their interactions. The forces between atoms are described by the Lennard-Jones potential[62]

$$V(r) = 4\,\varepsilon\left[\left(\frac{\boldsymbol{\sigma}}{r}\right)^{12} - \left(\frac{\boldsymbol{\sigma}}{\boldsymbol{r}}\right)^{6}\right] \qquad \text{Equation 5}$$

where ε and σ are specific Lennard- Jones parameter, different for different interacting particles. When the separation r is very small, the *1□12* term dominates, and the potential

is strongly positive. The $1/r^{12}$ term describes the potential due to the distortion of the electron clouds at small separations (the short-range repulsive tail). In contrast, the $1/r^{6}$ term predominates when the separation r increases in magnitude. Hence this term describes the long-range attractive tail of the potential between two particles.

*Components of AFM*

The basic components of an AFM are shown in **Figure 2.4**. The instrument consists of a piezoelectric scanner that moves along the sample in the X, Y, and Z directions. Attached to the end of the scanner is the cantilever and tip. It is the displacement of the probe tip at the end of the cantilever that is measured. A laser is focused onto the back of the cantilever, and as the tip scans the surface of the sample, the laser beam bounces off the cantilever and into a split photodiode detector. The difference in light intensities between the upper and lower photodiodes is sent to the photodetector, and then to the feedback loop. The feedback loop works by trying to keep the cantilever deflection constant by maintaining a constant distance between the cantilever and the sample. In order to maintain a constant distance, the scanner is moved to each X,Y position in the Z direction, therefore, adjusting the voltage applied to the scanner. The voltage is then converted to a cantilever deflection.

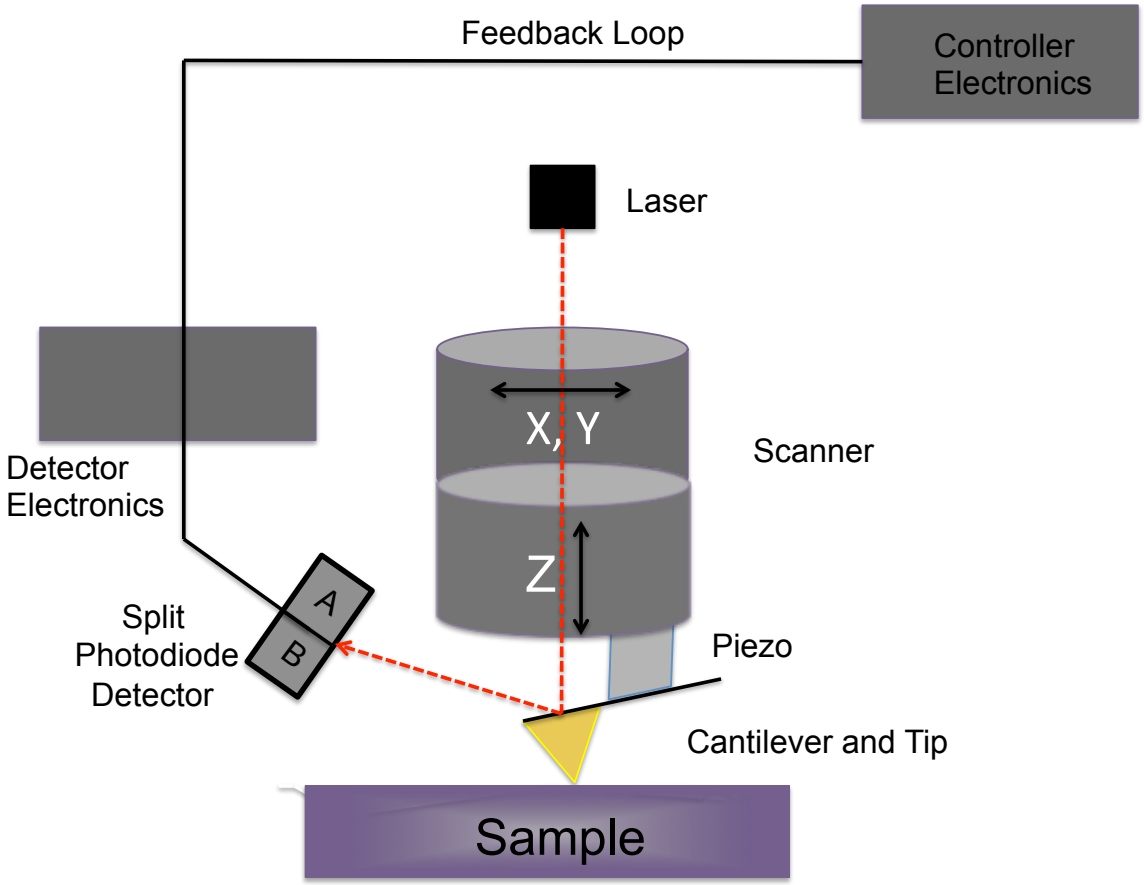


**Figure 2.4** Schematic of the AFM instrument

*AFM Modes*

An AFM can operate in two modes: constant force or constant height mode. In constant force mode, the cantilever height is effectively adjusted continuously so that a constant tip-sample interaction force is maintained, while constant height mode monitors variations in the cantilever deflection as the tip scans the surface. Constant force mode is more widely used because it provides a more accurate reading of sample topography.

Constant force mode can be separated further into contact and tapping. In contact mode, the tip always exerts a mechanical force of the sample. The cantilever is treated as spring, and Hooke's law can calculate the force,[62]

$$F = -kx \qquad \text{Equation 6}$$

Where F is force, k is the spring constant, and x is tip deflection. The separation distance is the sum of the tip deflection and the sample displacement. Applying constant force on the cantilever can lead to damage. An alternative contact approach is tapping mode in which an oscillating tip reduces the rate of energy dissipation at the sample surface by making intermittent contact (tapping surface). Tapping mode depends on the material properties of the sample and the interaction forces between the tip and the sample. Therefore, frequent calibration of the system must occur.

The attractive and repulsive forces between the tip, substrate, and sample can lead to discrepancies in the height profile. When the tip starts to approach the sample, the amplitude decreases linearly. In this regime, long range attractive forces are responsible for the oscillation damping. At a certain tip-sample separation a jump occurs in the amplitude. This jump marks the onset of a region where both the long range attractive and short range repulsive forces act on the tip. After the jump, the damping of the oscillation increases further, but this time net repulsive forces characterize the tip sample interaction. It is in the repulsive region that a more precise measure of the height can be obtained. This can be achieved by calibrating the free amplitude (oscillation of tip before

interaction with the substrate) of the cantilever using amplitude versus z piezo displacement curves.

## Experimental Section

### *Synthesis*

Germanane was synthesized by reacting β-$CaGe_2$ in aqueous HCl at -40 $^{o}$C for 8 days. 2-6 mm crystals of β-$CaGe_2$ were first synthesized by sealing stoichiometric ratios of calcium and germanium in a quartz tube and annealing at 950 - 1050 $^{o}$C, and slowly cooling down over a period of 2 - 10 days. After deintercalation, the product was filtered washed with methanol to remove residual $CaCl_2$, yielding 2-3 mm crystallites of GeH (**Figure 2.1a**).[47]

### *Exfoliation and Detection*

Substrates were prepared by cutting substrates into 3x3 to 5x5 mm squares and sonicating in acetone and isopropanol for 20 minutes each. The samples were dried with nitrogen containing blowgun and plasma cleaned (Harrick Plasma) for 30 minutes. Exfoliated sheets were detected using an Olympus Microscope equipped with Optical View camera.

### *AFM Analysis*

Heights of the single sheets were investigated using a Bruker AXS Dimension Icon AFM with ScanAsyst. The tips were high resolution tapping mode tips (RTESPA), which use a rotated tip to provide a more symmetric representation of features over 200 nm.

## Results and Discussion

### *Synthesis*

The purity of the $CaGe_2$ crystals was confirmed via powder X-ray diffraction (**Figure 2.5a**).[47] X-ray diffraction analysis of GeH (**Figure 2.5b**) confirms that it can be fit to a 2H unit cell (2 GeH layers per hexagonal unit cell spacing) with a = 3.880 Å and c = 11.04 Å (5.5 Å per layer). Compared to the original $CaGe_2$ unit cell parameters of a = 3.987, c = 30.0582, (6 layer stacking, c/6 = 5.097 Å) the hydrogen-terminated germanane is slightly contracted in the a-direction but expanded in the c-direction due to the replacement of $Ca^{2+}$ with 2 Ge–H bonds between each layer.[47] These lattice parameters do not correspond to any of the previously reported allotropes of germanium.

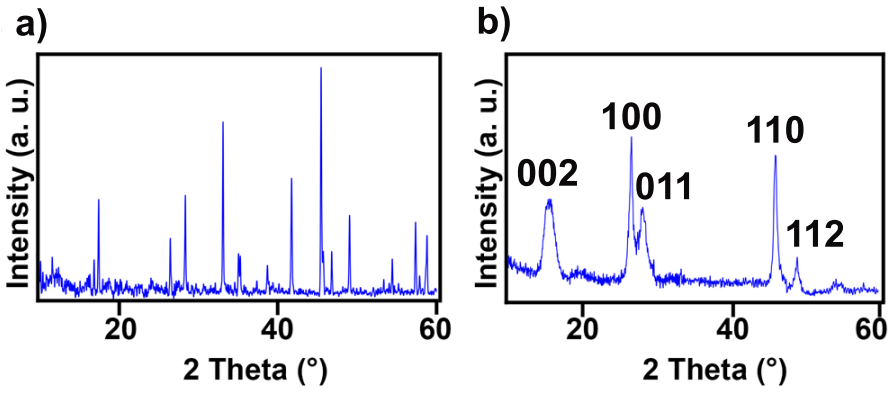


**Figure 2.5** Powder XRD pattern of a) $CaGe_2$ and b) GeH

Transmission electron microscopy analysis of the product shows that it has a layered morphology, with individual layers having less contrast than the 10 nm lacey carbon support grid (**Figure 2.6a,b**).[47] Energy dispersive X-ray analysis shows a strong Ge signal, an absence of Ca and O signals and the presence of residual Cl. The Cl:Ge ratio was calculated to be (2:98) (**Figure 2.6c**). Electron diffraction analysis of the layered material shows that crystallinity of the framework is preserved upon HCl treatment and there is a strong registration in the stacking between each layer. **Figure 2.6d** shows an electron diffraction pattern taken orthogonal to the layers, showing a hexagonal arrangement of diffraction peaks that occur in the a, b directions. The 3.87 Å spacing of the first set of hexagonal reflections is inconsistent with that of Germanium, and is indicative of an entirely different crystal structure. The GeH pattern can be indexed to a simple hexagonal unit cell with a = b = 3.87Å, assuming a [001] zone axis.

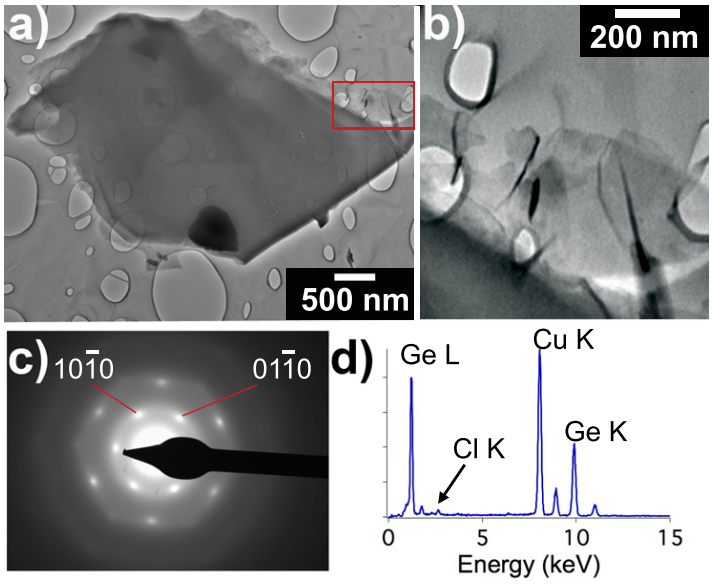


**Figure 2.6** a) Low magnification and b) Magnificd TEM micrograph of GeH platelets c) Electron diffraction pattern of platelets collected down the 0001 zone axis d) Energy dispersive X-ray spectroscopy of the GeH sheets.[47]

Fourier transform infrared spectroscopy and Raman spectroscopy were performed on GeH to confirm hydrogen termination (**Figure 2.7**). Transmission mode FTIR (**Figure 2.7a**) show extremely strong Ge—H stretching and multiple bending modes at ~2010 $cm^{-1}$ and 570, 507, and 475 $cm^{-1}$, respectively. Additionally, weak vibrational modes at 770 and 825 $cm^{-1}$ are also observed. These two vibrations also occur in the spectra of amorphous $Ge_{0.7}$:$H_{0.3}$ thin films and have been assigned by M. Cardona et al. to originate from bond-bending Ge—$H_2$ modes from nearest neighbor Ge atoms.[63,64] Thus, these two vibrations were assigned to Ge—$H_2$ bond-bending modes from neighboring Ge atoms the edges of each crystalline germanane sheet and/or the Ge—$H_2$ bonds within the lattice arising from Ge vacancies. From Raman spectroscopy (**Figure 2.7b**), the main Ge—Ge stretch in GeH occurs at 302 $cm^{-1}$, which is slightly blue-shifted compared to the 297 $cm^{-}$

[1] $E_2$ Raman mode for crystalline germanium. In addition, a second vibrational mode emerges at 228 $cm^{-1}$.[47]

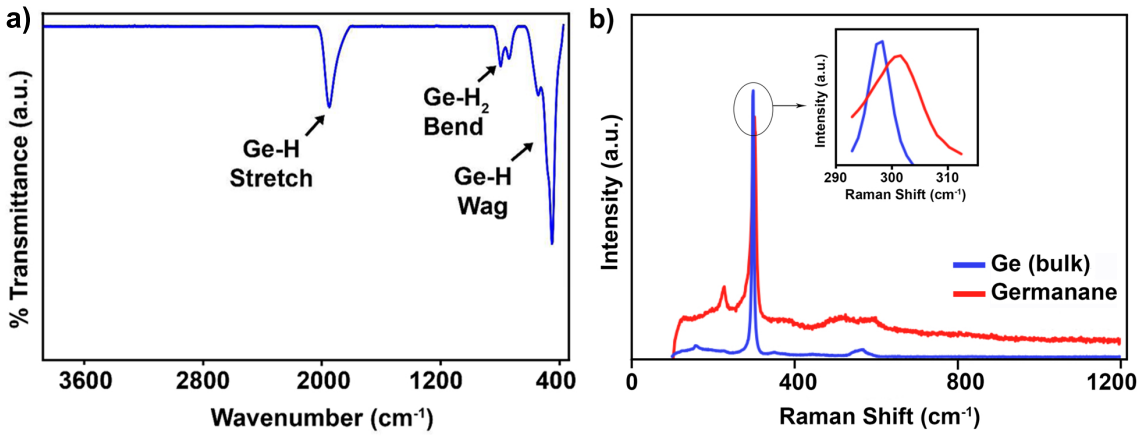


**Figure 2.7**a) Transmission-mode FTIR of GeH b) Raman spectrum of GeH (red) and Ge powder (blue), highlighting the difference in energy of the $E_2$ peak between GeH and Ge.[47]

*Exfoliation and Detection*

Single layer exfoliation of GeH was achieved on 100nm thick SiO2/Si substrate (**Figure 2.8b(inset)**). The exfoliated sheet is about 2 x 2 μm in length with an observed height of 0.6 nm (6 Å) (**Figure 2.8b**). Differences in the interactions between the AFM tip, the substrate, and the sample causes the measured AFM thickness to be larger than the expected value (0.81 nm) (**Figure 2.8a**). The free amplitude was calibrated for the sample and substrate for each sample (**Figure 2.9**). For the isolated single layer GeH, the free amplitude was 26 nm and 22 nm for the substrate and sample, respectively (**Figure 2.9a**).

The free amplitude was set at 22 nm to obtain the most accurate height profile for the single layer.

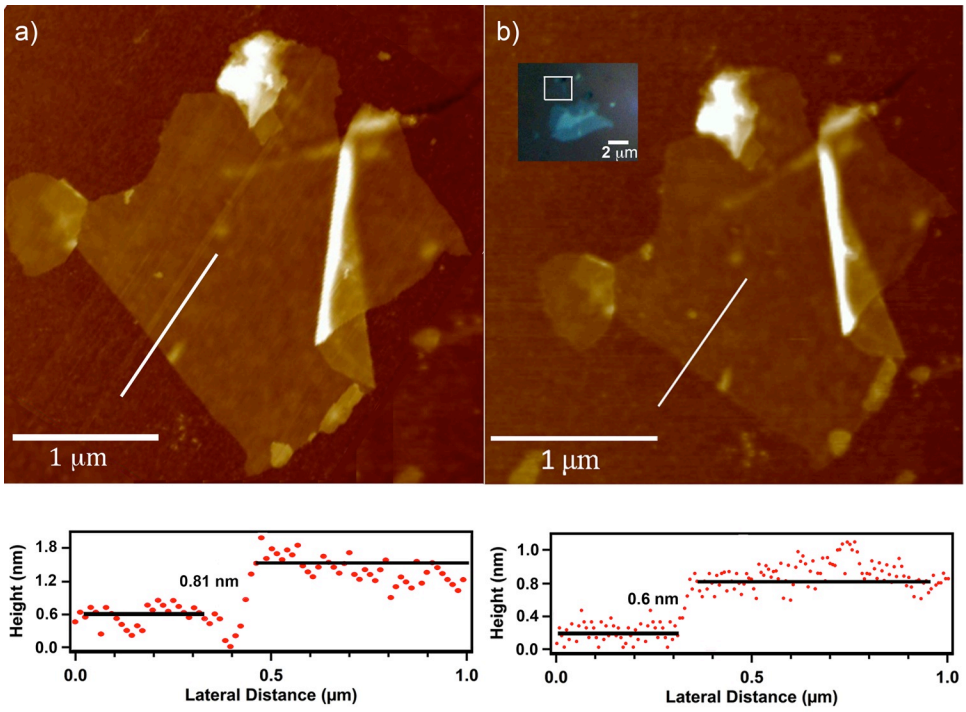


**Figure 2.8** a) AFM image of the uncalibrated single layer GeH (top), height profile of the uncalibrated single layer (bottom) b) AFM image of the calibrated single layer GeH (top), height profile of the calibrated single layer (bottom), optical image of single layer GeH on 100 nm thick $SiO_2$/Si substrate (inset)

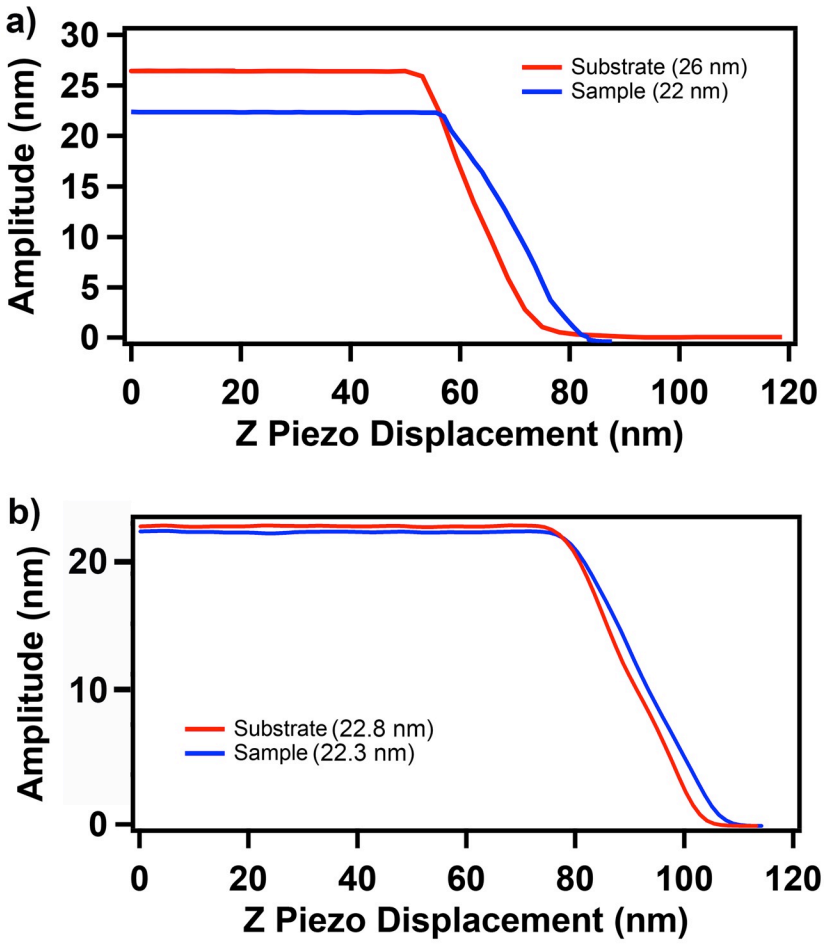


**Figure 2.9** a) Calibration plot of the isolated single layer GeH b) Calibration plot of the multilayer GeH sample

While PDMS exfoliation is the preferred method for obtaining single sheets of GeH, PDMS adheres to the sample and substrate. Removal of PDMS was achieved using lithium phenylacetylide, an organolithium reagent. The substrate was place in the solution for 1 hour, rinsed in $HCl/H_2O$ and isopropanol, and then dried with Ar gas in blowgun. **Figure 2.10** shows the AFM images of multilayer GeH before and after lithium phenylacetylide treatment. An accurate reading of the single sheet in **Figure 2.10a** cannot

be obtained because of the presence of PDMS. After treatment with lithium phenylacetylide, single and bilayer GeH can be measured more accurately. **Figure 2.10b** shows the calibration plot of the multilayer sample. The free amplitude was calibrated to be a 0.5 nm difference, meaning that the repulsive interaction between the tip and sample and the tip and substrate are similar.

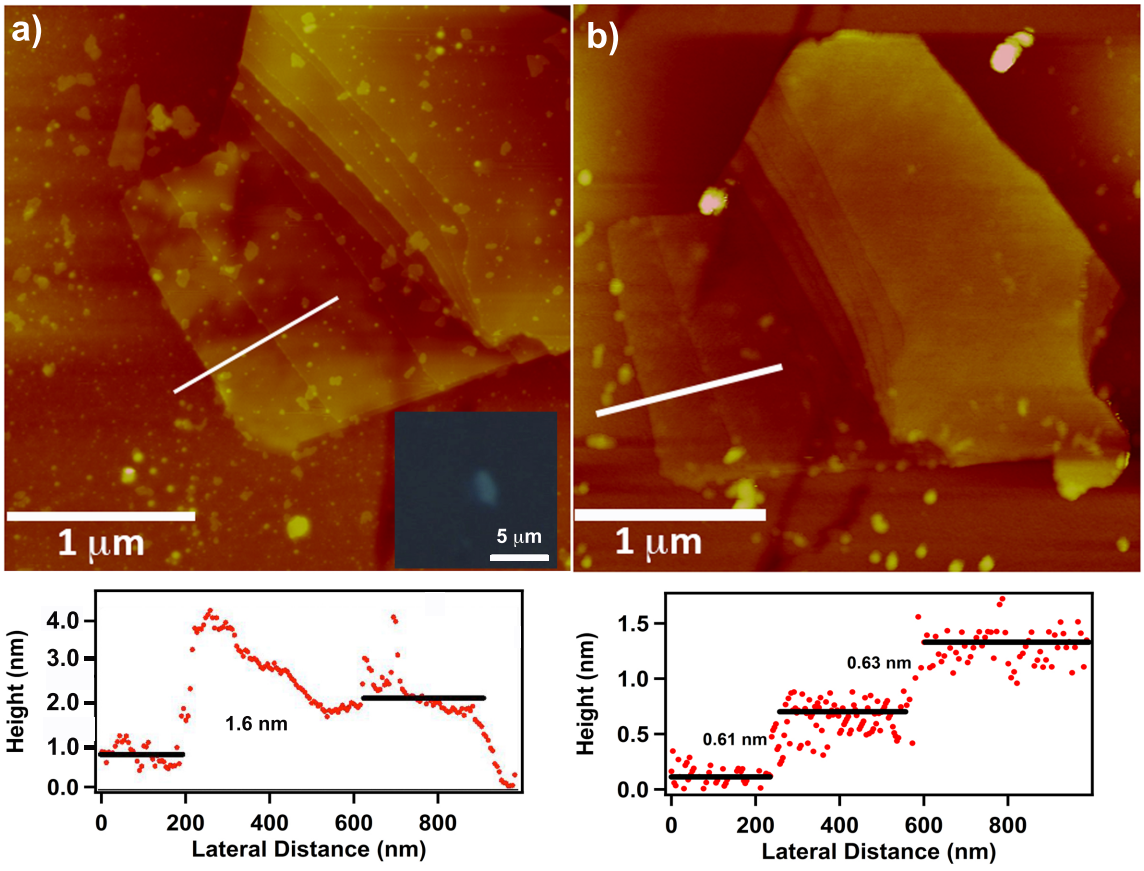


**Figure 2.10** a) AFM image of multilayer GeH contaminated with PDMS (top), height profile (bottom), optical image of sample on 100 nm thick $SiO_2$/Si substrate (inset) b) AFM image of multilayer GeH post treatment with lithium phenylacetylide, height profile (bottom)

Summary

In this study, we report on the PDMS based mechanical exfoliation of layered GeH to produce single to few layer GeH sheets. The exfoliated sheets were observed on 100 nm $SiO_2$/Si substrate under an optical microscope. An accurate height of the exfoliated GeH sheets was obtained using AFM. PDMS can be removed from the surface of the sample and substrate by using an organolithium reagent. This material represents a new class of covalently terminated single atom thick graphane analogues and has great potential for a wide range of optoelectronic and sensing applications.

# Chapter 3: Air Stability Studies on Bulk Germanane

## Overview

In this chapter the air stability of GeH will be explored. Information on the surface layers of solid materials is vital for nanotechnology, energy efficient systems, and energy storage. It is the surface that interfaces with its environment. The surface reactivity determines how well the material behaves in its intended function. It is therefore vital that the surface properties and behavior of materials used are thoroughly understood. ATR-FTIR spectroscopy can be used to analyze the surface chemistry of many types of systems. Here, the Ge—H vibrational mode was probed over 60 days. XPS is the surface technique used to probe the oxidation states present on the GeH surface. The samples were exposed to air for 1 day, 1 month, 5 months, and etched at 5 months to see if oxide could be removed.

## Introduction

The surface of semiconducting material exhibits a variety of chemical, structural, and electronic properties when exposed to different environments. A detailed characterization and understanding of these properties is required to fully utilize these materials in device and circuit applications. The formation of oxide on the compound's surface could possibly create problems during device fabrication. Knowing what specific oxides are present on the surface and how to remove them is of obvious benefit in characterizing the interface and understanding its behavior.

Attenuated Total Reflectance Spectroscopy

ATR-FTIR spectroscopy can be used for the study of surfaces due to its sensitivity to the surface of the sample. ATR is based on the phenomenon of total internal reflection in which an evanescent wave is formed on the other side of a reflecting interface.

An absorbing material (medium 2) is brought into contact with a totally reflecting interface (medium 1) and absorbs some of the intensity of the evanescent wave causing the intensity of the reflected light to attenuate with respect to the incoming intensity. The incident light is totally reflected if the angle of incidence is larger than the critical angle given by:

$$\theta_c = sin^{-1}\frac{n_2}{n_1} \qquad \text{Equation 7}$$

where $n_1$ is the refractive index of medium 1, and $n_2$ is the refractive index of medium 2. At $\theta_1 > \theta_c$, the amplitude of the light in medium 2 is expressed as:

$$E = E_0 \exp(-\gamma d) \qquad \text{Equation 8}$$

$$\gamma = \frac{2\pi n_1}{\lambda_1}\sqrt{sin^2\theta_1 - \left(\frac{n_2}{n_1}\right)^2} \qquad \text{Equation 9}$$

where $E_0$ is the amplitude of the electric field at the interface between media 1 and 2, □ is the decay coefficient, d is the distance from the surface, and □*1* is the wavelength of medium 1. This equation shows the behavior of the light in a transparent medium (2) under the conditions of total reflection. As the light penetrates into medium 2, the

amplitude decays exponentially, but there is no loss of energy since the loss of energy in the sample is proportional to $k|E|^2$. This wave is called an evanescent wave. The penetration depth of the evanescent wave is defined as the depth at which the field strength falls to 1/e of its initial value:

$$d_p = \frac{1}{2\pi\bar{\nu}\sqrt{n_1^2 sin^2\theta_1 - n_2^2}} \qquad \text{Equation 10}$$

where $\bar{\nu}$ is the energy (in wavenumbers) of the incident radiation, θ is the incidence angle, $n_1$ and $n_2$ are the refractive indices of the reflecting interface and the sample, respectively.

To analyze a sample by ATR, the sample is brought into intimate contact with the ATR element. There are many ATR elements such as germanium, silicon, ZnSe, and diamond. Diamond is the most favorable because of its robustness and strong infrared transparency. The evanescent wave extends just a short distance above the surface of the ATR element- typically on the order of the wavelength of light used for the measurement. The sample needs to fill the small volume above the interface that is probed by the evanescent wave. If only a fraction of that volume is filled by the sample, the absorption experienced by the evanescent wave is smaller than if the volume is filled completely. **Figure 3.1** depicts the mechanics of an ATR diamond crystal.

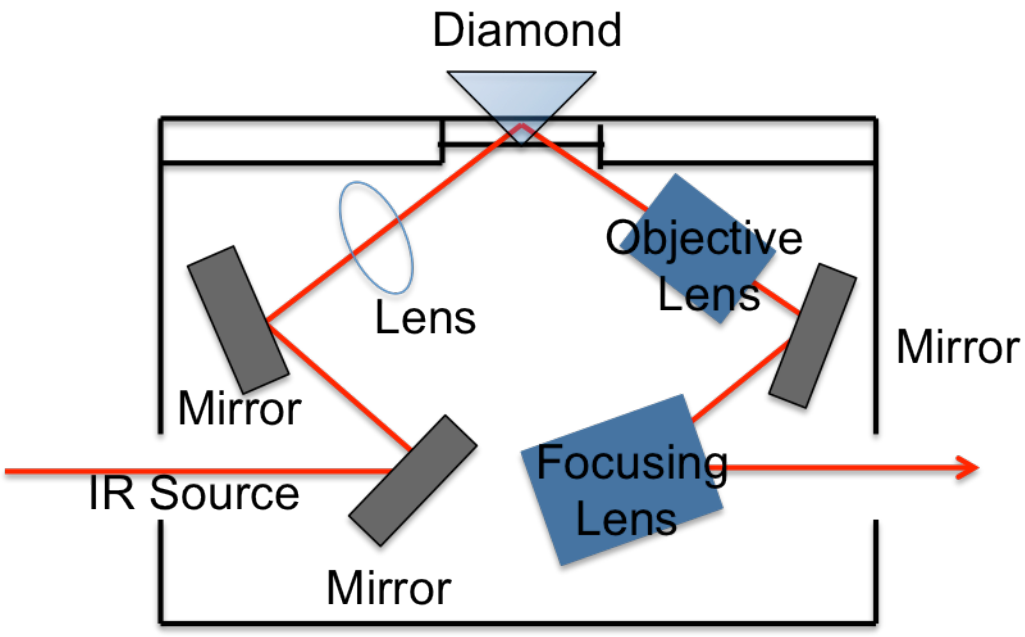


**Figure 311** Schematic diagram of diamond ATR setup

The ATR spectra have a wavelength dependence in which ATR spectra are less intense at shorter wavelengths and more intense at longer wavelengths relative to transmission spectra of the same material. Distortion can be minimized by using a high index of refraction reflecting interface and using higher angles of incidence that are as far from the critical angle as possible. Computer software has been developed to correct for this distortion and make ATR spectra appear more like transmission spectra by multiplying each point of absorbance in the spectrum by a factor, such as $\lambda_{ref}/\lambda$.

X-ray Photoelectron Spectroscopy

XPS is a powerful tool for surface analysis that is able to provide accurate qualitative elemental analysis (except H and He), quantitative composition, and determine the

chemical state of species (binding and oxidation). The information it provides is for the top 10 nm of the surface. XPS (originally coined Electron Spectroscopy for Chemical Analysis/Applications) was made commercially available in 1969. It is based on the photoelectric effect in which the interaction of an X-ray photon of sufficient energy with a solid results in emission of the electrons from its surface without energy loss (**Figure 3.2a**). In XPS, the sample under ultra high vacuum is irradiated with a monochromatic X-ray source of sufficient energy to eject core electrons to vacuum where they are collected by the analyzer and sorted by kinetic energy. The process can be described by:[62]

$$h\nu = E_B + E_K + \phi \qquad \text{Equation 11}$$

where $h$□ is the energy of the X-ray source (known value), □□ is the binding energy of the electron in the atom, □□ is the kinetic energy of the emitted electron, and □ is the work function of the specific spectrometer. □□ provides us with the valuable information about the photoemitting atom.

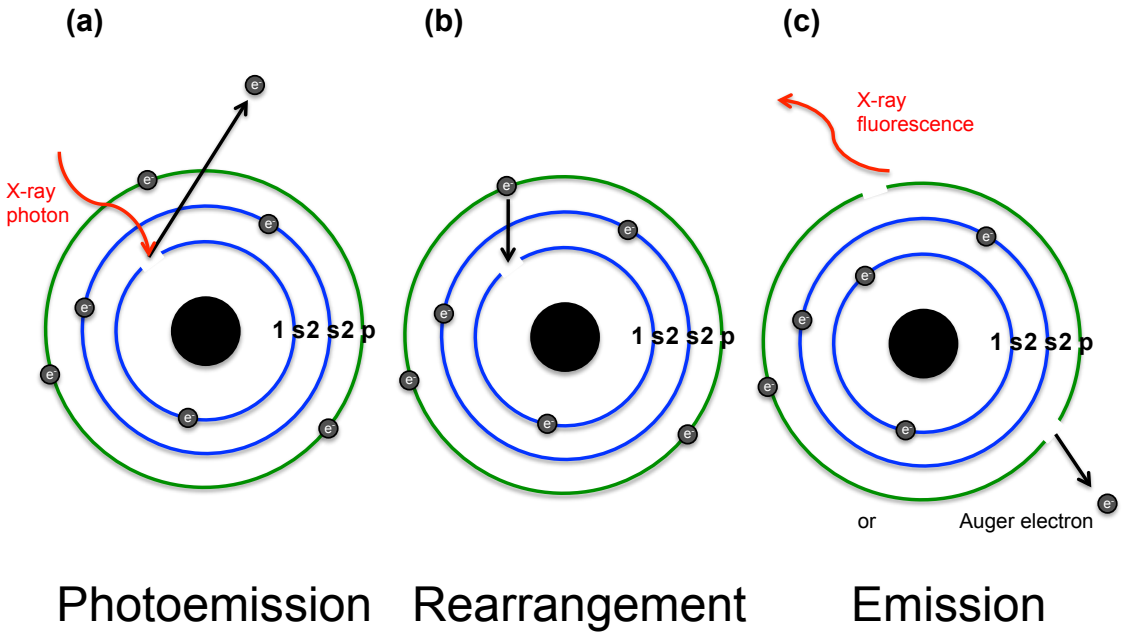


**Figure 3.2** a) Photoionization process: X-ray photon excites core level electron leading to photoemission b) Rearrangement: An electron from a higher energy level drops to fill the vacant core hole c) Emission: Excess energy from rearrangement can cause either the ejection of an electron from a higher energy level (Auger process) or emission of an X-ray photon, a process called X-ray fluorescence

The binding energy of an electron in an atom varies with type of atom and the type of atoms bound to it (bound atoms will alter the electron distribution on the atom of interest). Therefore, variations in the binding energy will only be detected for covalent and ionic bonds between atoms. These changes are called chemical shifts and they can be explained using Koopmans' theorem. Koopmans' theorem states that the binding energy of an emitted photoelectron is simply the energy difference between the (n-1) electron finale state and the n-electron initial state: [62]

$$E_B = E_f(n-1) - E_i(n) \qquad \text{Equation 12}$$

where □□□−*I* is the final state energy and □□□ is the initial state energy. If no electrons undergo rearrangement (**Figure 3.2b**) during the photoemission process, then the observed binding energy would be the negative kinetic energy for the ejected photoelectron. Koopmans' theorem then becomes: [62]

$$\Delta E_B = -\Delta E_K \qquad \text{Equation 13}$$

where Δ□□, the chemical shift, is the change that the initial state undergoes during the photoemission process.

*Components of XPS*

The primary components of a XPS system are the vacuum, X-ray source, electron energy analyzer, and the data system (**Figure 3.3**). The sample is analyzed in the main vacuum chamber because the emitted photoelectrons must be able to travel from the sample through the analyzer to the detector without colliding with gaseous particles. Some components such as the X-ray source require vacuum conditions to remain operational. Vacuum conditions are also necessary to ensure that the surface composition of the sample under investigation does not change during the experiment. Samples are introduced into the analysis vacuum chamber via a load lock chamber. The sample is evacuated and transferred into the analytical chamber. The sample must then be properly positioned for analysis which is done by a sample manipulator that moves in X, Y, and Z direction.

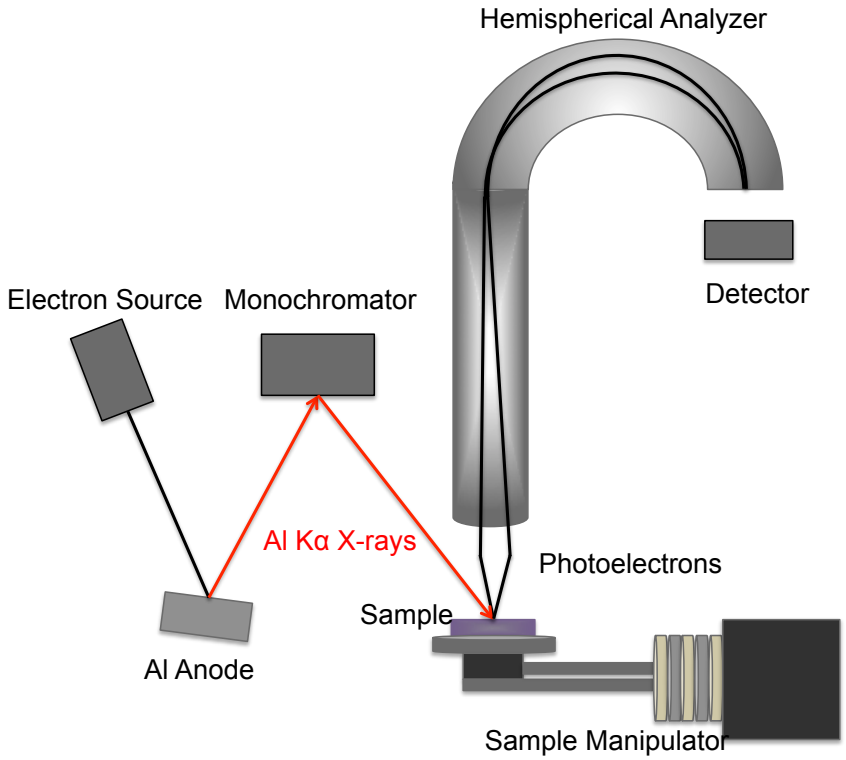


**Figure** Error! No text of specified style in document.**12** Components of XPS

The X-ray sources for XPS are usually produced by impinging high energy (~10keV) electron beam onto a target.[62] Core holes are created in the atoms of a target material which in turn emits flu. X-rays and electrons (**Figure 3.2c**). It is the fluorescence X-rays that are used. The most common X-ray sources are Mg and Al. A specific fluorescence line is used instead of the background emission since its intensity is several orders of magnitude higher than the background emission. Thus, the X-ray emission energy is fixed for each source. The area of the sample irradiated by the X-ray source depends on the geometry of the source and the type of electron gun used to stimulate X-ray emission.

Spot sizes of <50 mm in diameter can be achieved when using a focused electron gun and the quartz crystal used as monochromator and focusing element.

Electrostatic hemispherical analyzer is commonly used in XPS instruments. The electrons are deflected by an electrostatic field. A potential is placed across the hemispheres such that outer arch is negative and the inner is positive with respect to the center line. The center line is the pass energy. Typically 20 eV pass energies are used to acquire high res XPS and 80 eV used to acquire survey scans. ~10% of the pass energy range of electron energies that can successfully travel from the entrance to the exit of the analyzer without undergoing a collision with one of the hemispheres. The electrons are counted once they have passed through the energy analyzer. Multichannel array detector is used to count the number of electrons leaving the analyzer at each energy.

XPS analyses are performed by taking a wide scan or survey scan spectrum, and then looking in more detail over a smaller range at specific features found in the survey scan spectrum (**Figure 3.4**). The number of counts attributed to the background typically increases at first and then decreases slowly with increasing binding energy (decreasing kinetic energy) above the photoemission peak. This is due to inelastic scattering. The magnitude and dependence of the inelastically scattered background intensity with increasing binding energy will depend on the composition and structure of the sample as well as the photoemission peak being analyzed. There is a continuum of energies of the inelastic background electrons that range from the photoemission peak kinetic energy of the photoelectron to zero kinetic energy, since the collision events reduce the kinetic energy of the photoelectron do not have discrete energies.

Also found in the background of survey scans are Auger peaks. Auger electrons are associated with energy transitions within an atom after excitation by an incident X-ray photon (**Figure 3.2c**). The Auger peaks can be separated from the photoelectron spectrum by recording two different photon excitation energies. The Auger peaks will always appear in the same position, but the photoemission lines will be shifter by the energy difference between the energies of the two incident X-ray beams used to excite the signal.

*Quantification*

In order to maximize the information extracted from a XPS spectra the area and binding energy of each peak must be determined. This requires the use of peak-fitting software (CasaXPS). Parameters to consider are the background (linear or Shirley), peak shape (Gaussian, Lorentzian, asymmetric, or a mixture), peak position, peak height, and peak width. After a suitable inelastic background subtraction, the area of the peaks can be determined.

*Relative Sensitivity Factors*

When the quantitative compostition of a sample is to be determined, the relative sensitivity factors are applied. RSFs are used to scale the measured peak area so that variations in the peak areas are representative of the amount of material in the sample surface. These factors can be calculated either experimentally or theoretically.[62] However, experimentally determined sensitivity factors data sets were published by several research groups.[65-71]

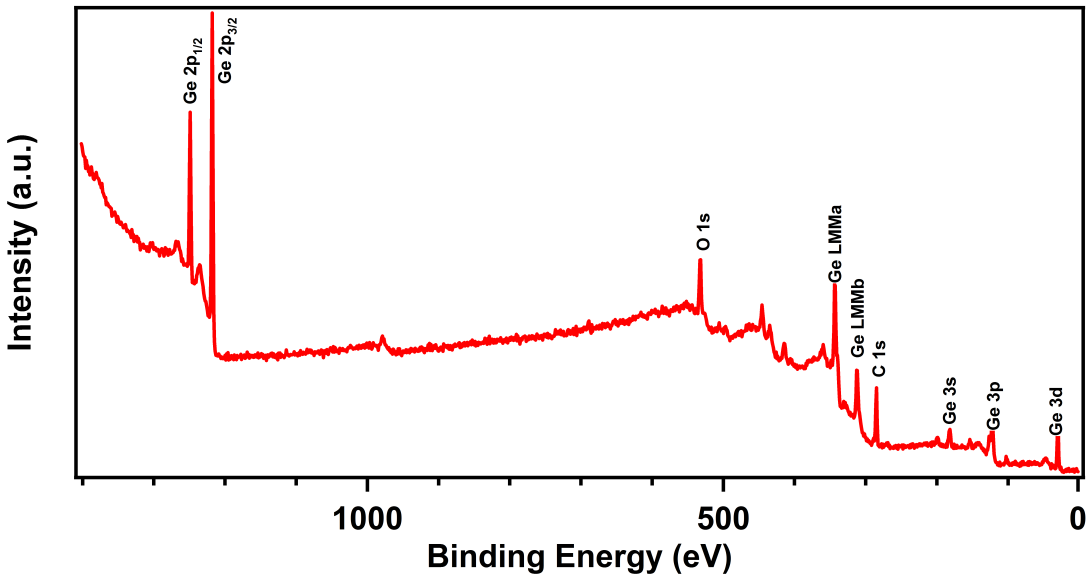


**Figure 13** Survey of Germanane

Experimental Section

*Sample Preparation*

The samples used in this chapter were synthesized as previously stated and analyzed as prepared after 1 day, 1 month, and 5 months exposure to air. GeH powder was placed on Carbon tape and placed in an air-free holder to be loaded in the XPS sample analysis chamber.

*Analysis Conditions*

XPS analysis was performed using a Kratos Axis Ultra XPS with a monochromatic Al gun (1486. 6 eV). The pressure was $10^{-9}$ Torr in the Surface Analysis Chamber. The

instrument was calibrated by setting the C1s line to 284.6 eV binding energy. Survey scans were collected using 80 eV pass energy and regions collected at 40 eV. An Ar ion gun was used to etch the surface to remove oxide from the surface. At 2.2 keV for 90 seconds, 0.5 nm of the surface was etched.

*Data Analysis*

Spectra were processed using Computer Aided Surface Analysis for X-ray Photoelectron Spectroscopy (CasaXPS). Peak area intensity data were obtained after Shirley background subtraction, and using a Lorentzian-Gaussian line shape.

Results and Discussion

*ATR-FTIR Analysis*

ATR-FTIR is sensitive probe for the presence of Ge—O and Ge—H bonds, so time dependent ATR-FTIR study was conducted to determine if Ge—O vibrational modes in the 800-1000 $cm^{-1}$ range emerge after exposure to an ambient atmosphere. After 60 days there was no change in this range, proving that the bulk GeH resists oxidation (**Figure 3.5)**

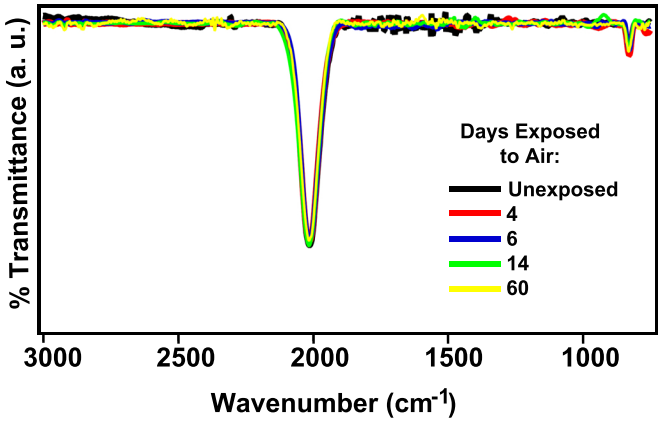


**Figure 3.14** ATR-FTIR spectrum of time dependent anaylsis of GeH over 60 days

*X-ray Photoelectron Spectroscopy Analysis*

The surveys for the 1 day sample and the 5 month sample before and after etching is shown in **Figure 3.6**. After etching the survey shows a decrease in the O 1s peak (532 eV). **Figure 3.7** shows the XPS spectra of germanium powder with surface oxide, GeH exposed to air for one day, 1 month, 5 months, and a 0.5nm etch of 5 month exposed GeH. The areas were quantified to obtain an accurate measure of percent concentration for each oxidation of germanium present. The percent concentrations are reported in **Table 3.1**.

Germanium powder with surface oxide contains the most oxidation states: elemental germanium, $Ge^{0}$ (1216.96 eV), 2 sub-oxides, $Ge^{2+}$ and $Ge^{3+}$ (1218.86 and 1220.19 eV, respectively), and germanium dioxide, $Ge^{4+}$ (1221.4 eV). After exposure to air for one day, there is only one oxidation state present, which corresponds to $Ge^{1+}$ (1217.81 eV), the oxidation state of GeH. When left out in air for 1 month, 19.46% of the GeH surface is covered by sub-oxide (1219.25 eV). 5 months later, the sub-oxide has grown to

26.32%. Fortunately, it is only surface contamination as seen by a 0.5 nm etch of the 5 month exposed sample. The percent concentration decreases to 10.12%, which means with further etching, the concentration of sub-oxide can be decreased to zero and return the sample back to 1day exposure GeH.

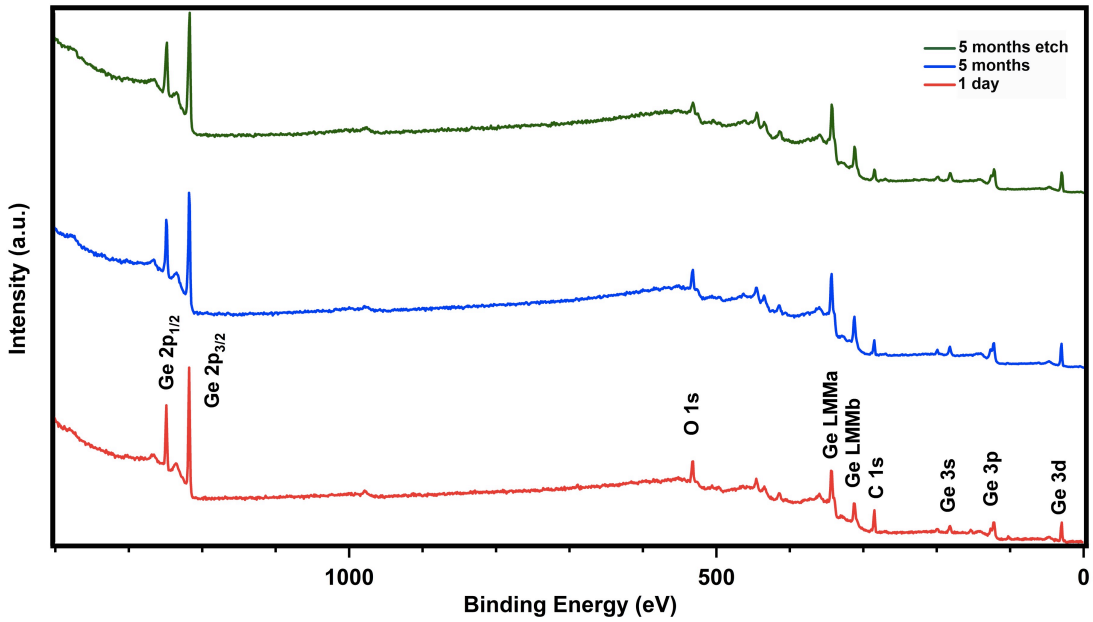


**Figure 3.15** Surveys for GeH samples exposed in air for 1 day (red), 5 months (blue), and etched after 5 months (green)

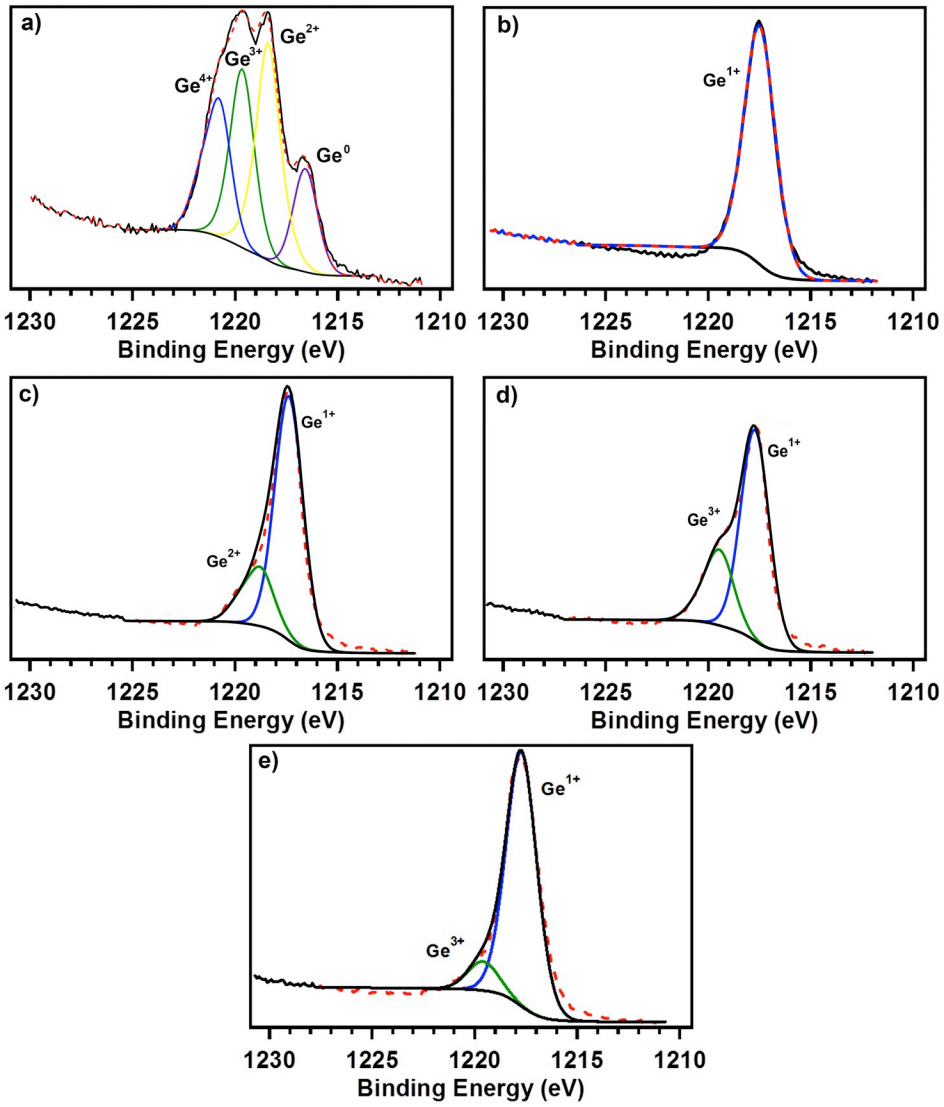


**Figure 3.16** XPS spectra of a) germanium powder with surface oxide b) GeH exposed to air for 1 day c) GeH exposed to air for 1 month d) GeH exposed to air for 5 months e) 0.5 nm etch of 5 month GeH

| Oxidation State | Ge with Surface Oxide (%) | 1 day GeH (%) | 1 month GeH (%) | 5 month GeH (%) | 5 month GeH etched (%) |
|---|---|---|---|---|---|
| $Ge^{4+}$ | 20.83 | -- | -- | -- | -- |
| $Ge^{3+}$ | 27.88 | -- | 19.46 | 26.32 | 10.12 |
| $Ge^{2+}$ | 35.47 | -- | -- | -- | -- |
| $Ge^{1+}$ | -- | 100 | 80.54 | 73.68 | 89.88 |
| $Ge^{0}$ | 15.82 | -- | -- | -- | -- |

**Table 3.1** Percent Concentration of each Ge oxidation state

Summary

In this study, the air stability of bulk GeH was investigated using ATR-FTIR spectroscopy and XPS. Using ATR-FTIR, we observed no change in the Ge—H stretch and no appearance of a Ge—O bond over 60 days. XPS analysis shows that there is a presence of surface oxide on GeH. However, after etching away the surface layers, the presence of oxide is reduced. This means that the GeH structure remains intact, and does not undergo any major chemical change when exposed to air.

# Chapter 4: Conclusions

In summary, single layer exfoliation of germanane was achieved using PDMS mechanical exfoiliation on a 100 nm thick $SiO_2$/Si substrate. PDMS can be removed from the sample by treatment in a lithium phenylacetylide solution. Sub-oxides are present on the surface of the GeH, however, they can be removed allowing for GeH to be developed for optoelectronic applications.

# References


(1) Guettinger, J.; Molitor, F.; Stampfer, C.; Schnez, S.; Jacobsen, A.; Droescher, S.; Ihn, T.; Ensslin, K. Transport through Graphene Quantum Dots. *Reports on Progress in Physics* **2012**, *75*.

(2) Schweizer, H.; Jetter, M.; Scholz, F. Quantum-Dot Lasers In *Single Quantum Dots: Fundamentals, Applications and New Concepts*; Micheler, P., Ed. 2003; Vol. 90, p 185-235.

(3) Semonin, O. E.; Luther, J. M.; Beard, M. C. Quantum Dots for Next-Generation Photovoltaics. *Materials Today* **2012**, *15*, 508-515.

(4) Dong, L.; Chu, Y.; Zhang, Y. Micro Emulsion-Mediated Solvothermal Synthesis of Zns Nanowires. *Materials Letters* **2007**, *61*, 4651-4654.

(5) Mao, S. S. Nanolasers: Lasing from Nanoscale Quantum Wires. *International Journal of Nanotechnology* **2004**, *1*, 42-85.

(6) Novoselov, K. S.; Geim, A. K.; Morozov, S. V.; Jiang, D.; Zhang, Y.; Dubonos, S. V.; Grigorieva, I. V.; Firsov, A. A. Electric Field Effect in Atomically Thin Carbon Films. *Science* **2004**, *306*, 666-669.

(7) Bednorz, J. G.; Muller, K. A. Possible High-Tc Superconductivity in the Ba-La-Cu-O System *Zeit. Fur. Phys. B* **1986**, *64*, 189-193.

(8) Kamihara, Y.; Hiramatsu, H.; Hirano, M.; Kawamura, R.; Yanagi, H.; Kamiya, T.; Hosono, H. Iron-Based Layered Superconductor: LaOFeP. *J. Am. Chem. Soc.* **2006**, *128*, 10012-10013.

(9) Wilson, J. A.; Yoffe, A. D. Transition Metal Dichalcogenides Discussion and Interpretation of Observed Optical, Electrical, and Structural Properties *Advances in Physics* **1969**, *18*, 193-335.

(10) Fuzellier, H.; Melin, J.; Herold, A. Electric-Conductivity of Lamellar Compounds - Graphite-Sbf5 and Graphite-Sbcl5. *Carbon* **1977**, *15*, 45-46.

(11) Thompson, T. E.; Falardeau, E. R.; Hanlon, L. R. Electrical-Conductivity and Optical Reflectance of Graphite-Sbf5 Compounds. *Carbon* **1977**, *15*, 39-43.

(12) Ubbelohde, A. R.; Lewis, F. A. *Graphite and Its Crystal Compounds*; Clarendon Press: Oxford, 1960.

(13) Bolotin, K. I.; Sikes, K. J.; Jiang, Z.; Klima, M.; Fudenberg, G.; Hone, J.; Kim, P.; Stormer, H. L. Ultrahigh Electron Mobility in Suspended Graphene. *Solid State Communications* **2008**, *146*, 351-355.

(14) Morozov, S. V.; Novoselov, K. S.; Katsnelson, M. I.; Schedin, F.; Elias, D. C.; Jaszczak, J. A.; Geim, A. K. Giant Intrinsic Carrier Mobilities in Graphene and Its Bilayer. *Physical review letters* **2008**, *100*, 016602-016602.

(15) Balandin, A. A.; Ghosh, S.; Bao, W.; Calizo, I.; Teweldebrhan, D.; Miao, F.; Lau, C. N. Superior Thermal Conductivity of Single-Layer Graphene. *Nano Letters* **2008**, *8*, 902-907.

(16) Lee, C.; Wei, X.; Kysar, J. W.; Hone, J. Measurement of the Elastic Properties and Intrinsic Strength of Monolayer Graphene. *Science* **2008**, *321*, 385-388.

(17) Begliarbekov, M.; Strauf, S.; Search, C. P. Quantum Inductance and High Frequency Oscillators in Graphene Nanoribbons. *Nanotechnology* **2011**, *22*.

(18) Britnell, L.; Gorbachev, R. V.; Jalil, R.; Belle, B. D.; Schedin, F.; Mishchenko, A.; Georgiou, T.; Katsnelson, M. I.; Eaves, L.; Morozov, S. V.*et al.* Field-Effect Tunneling Transistor Based on Vertical Graphene Heterostructures. *Science* **2012**, *335*, 947-950.

(19) Knoch, J.; Appenzeller, J. Carbon Nanotube Field-Effect Transistors-the Importance of Being Small In *Amiware Hardware Technology Drivers of Ambient Intelligence*; Mukherjee, S., Aarts, R., Roovers, R., Widdershoven, F., Ouwerkerk, M., Eds.; Springer Netherlands: 2006; Vol. 5, p 371-402.

(20) Majumdar, A.; Ren, Z. B.; Sleight, J. W.; Dobuzinsky, D.; Holt, J. R.; Venigalla, R.; Koester, S. J.; Haensch, W. High-Performance Undoped-Body 8-nm-Thin SOI Field-Effect Transistors. *Ieee Electron Device Letters* **2008**, *29*, 515-517.

(21) Pradhan, N. R.; Rhodes, D.; Zhang, Q.; Talapatra, S.; Terrones, M.; Ajayan, P. M.; Balicas, L. Intrinsic Carrier Mobility of Multi-Layered MoS2 Field-Effect Transistors on SiO2. *arxiv:1301.2813* **2013**.

(22) Radisavljevic, B.; Radenovic, A.; Brivio, J.; Giacometti, V.; Kis, A. Single-Layer MoS2 Transistors. *Nat Nanotechnol* **2011**, *6*, 147-150.

(23) Feng, J.; Qian, X.; Huang, C.-W.; Li, J. Strain-Engineered Artificial Atom as a Broad-Spectrum Solar Energy Funnel. *Nature Photonics* **2012**, *6*, 865-871.

(24) Mlinar, V. Engineered Nanomaterials for Solar Energy Conversion. *Nanotechnology* **2013**, *24*, 042001-042001.

(25) Wang, Q. H.; Kalantar-Zadeh, K.; Kis, A.; Coleman, J. N.; Strano, M. S. Electronics and Optoelectronics of Two-Dimensional Transition Metal Dichalcogenides. *Nat Nanotechnol* **2012**, *7*, 699-712.

(26) Kustra, S.; Wu, H.; Basu, S.; Rohde, G. K.; Bettinger, C. J. High-Throughput Arrays for Rapid Characterization of Solution-Processable Transparent Conducting Electrodes. *Small* **2012**, *8*, 3746-3751.

(27) Kim, K. S.; Zhao, Y.; Jang, H.; Lee, S. Y.; Kim, J. M.; Kim, K. S.; Ahn, J.-H.; Kim, P.; Choi, J.-Y.; Hong, B. H. Large-Scale Pattern Growth of Graphene Films for Stretchable Transparent Electrodes. *Nature* **2009**, *457*, 706-710.

(28) Yang, H.; Heo, J.; Park, S.; Song, H. J.; Seo, D. H.; Byun, K. E.; Kim, P.; Yoo, I.; Chung, H. J.; Kim, K. Graphene Barristor, a Triode Device with a Gate-Controlled Schottky Barrier. *Science* **2012**, *336*, 1140-1143.

(29) Stankovich, S.; Dikin, D. A.; Dommett, G. H. B.; Kohlhaas, K. M.; Zimney, E. J.; Stach, E. A.; Piner, R. D.; Nguyen, S. T.; Ruoff, R. S. Graphene-Based Composite Materials. *Nature* **2006**, *442*, 282-286.

(30) Frindt, R. F. Single Crystals of MoS2 Several Molecular Layers Thick *Journal of Applied Physics* **1966**, *37*, 1928-1929.

(31) Consador, F.; Fife, A. A.; Frindt, R. F.; Gygax, S. Construction and Properties of Weak-Link Detectors Using Superconducting Layer Structure *Appl. Phys. Lett.* **1971**, *18*, 233-235.

(32) Frindt, R. F. Supercondutivity in Ultrathin NbSe2 Layers *Physical Review Letters* **1972**, *28*, 299-301.

(33) Mak, K. F.; Lee, C.; Hone, J.; Shan, J.; Heinz, T. F. Atomically Thin MoS2: A New Direct-Gap Semiconductor. *Physical Review Letters* **2010**, *105*, 136805.

(34) Kuc, A.; Zibouche, N.; Heine, T. Influence of Quantum Confinement on the Electronic Structure of the Transition Metal Sulfide Ts2. *Physical Review B* **2011**, *83*.

(35) Lee, C.; Yan, H.; Brus, L. E.; Heinz, T. F.; Hone, J.; Ryu, S. Anomalous Lattice Vibrations of Single- and Few-Layer MoS2. *ACS Nano* **2010**, *4*, 2695-2700.

(36) Kubota, Y.; Watanabe, K.; Tsuda, O.; Taniguchi, T. Deep Ultraviolet Light-Emitting Hexagonal Boron Nitride Synthesized at Atmospheric Pressure. *Science* **2007**, *317*, 932-934.

(37) Murakawa, M.; Watanabe, S.; Miyake, S. Optical Properties of Cubic Boron Nitride Films Made by a Reactive Ion Plating Method. *Thin Solid Films* **1993**, *226*, 82-86.

(38) Museur, L.; Kanaev, A. Near Band-Gap Photoluminescence Properties of Hexagonal Boron Nitride. *Journal of Applied Physics* **2008**, *103*, 103520-103527.

(39) Li, C.; Bando, Y.; Zhi, C.; Huang, Y.; Golberg, D. Thickness-Dependent Bending Modulus of Hexagonal Boron Nitride Nanosheets. *Nanotechnology* **2009**, *20*, 385707-385707.

(40) Sichel, E. K.; Miller, R. E.; Abrahams, M. S.; Buiocchi, C. J. Heat-Capacity and Thermal-Conductivity of Hexagonal Pyrolytic Boron-Nitride. *Physical Review B* **1976**, *13*, 4607-4611.

(41) Simpson, A.; Stuckes, A. D. Thermal Conductivity of Highly Orientated Pyrolytic Boron Nitride. *Journal of Physics Part C Solid State Physics* **1971**, *4*, 1710-&.

(42) Watanabe, K.; Taniguchi, T.; Niiyama, T.; Miya, K.; Taniguchi, M. Far-Ultraviolet Plane-Emission Handheld Device Based on Hexagonal Boron Nitride. *Nature Photonics* **2009**, *3*, 591-594.

(43) Aufray, B.; Kara, A.; Vizzini, S.; Oughaddou, H.; Leandri, C.; Ealet, B.; Le Lay, G. Graphene-Like Silicon Nanoribbons on Ag(110): A Possible Formation of Silicene. *Appl. Phys. Lett.* **2010**, *96*, 183102.

(44) Lalmi, B.; Oughaddou, H.; Enriquez, H.; Kara, A.; Vizzini, S.; Ealet, B.; Aufray, B. Epitaxial Growth of a Silicene Sheet. *Appl. Phys. Lett.* **2010**, *97*, 223109.

(45) Kara, A.; Enriquez, H.; Seitsonen, A. P.; Voon, L.; Vizzini, S.; Aufray, B.; Oughaddou, H. A Review on Silicene - New Candidate for Electronics. *Surf. Sci. Rep.* **2012**, *67*, 1-18.

(46) Fleurence, A.; Friedlein, R.; Ozaki, T.; Kawai, H.; Wang, Y.; Yamada-Takamura, Y. Experimental Evidence for Epitaxial Silicene on Diboride Thin Films. *Physical Review Letters* **2012**, *108*, 245501.

(47) Bianco, E.; Butler, S.; Jiang, S.; Restrepo, O. D.; Windl, W.; Goldberger, J. E. Stability and Exfoliation of Germanane; a Germanium Graphane Analogue. *under review*.

(48) Vogg, G.; Brandt, M. S.; Stutzmann, M. Polygermyne - a Prototype System for Layered Germanium Polymers. *Advanced Materials* **2000**, *12*, 1278-1281.

(49) Okamoto, H.; Kumai, Y.; Sugiyama, Y.; Mitsuoka, T.; Nakanishi, K.; Ohta, T.; Nozaki, H.; Yamaguchi, S.; Shirai, S.; Nakano, H. Silicon Nanosheets and Their Self-Assembled Regular Stacking Structure. *J. Am. Chem. Soc.* **2010**, *132*, 2710-2718.

(50) Dahn, J. R.; Way, B. M.; Fuller, E.; Tse, J. S. Structure of Siloxene and Layered Polysilane (Si6h6). *Physical Review B: Condensed Matter and Materials Physics* **1993**, *48*, 17872-17877.

(51) Yamanaka, S.; Matsuura, H.; Ishikawa, M. New Deintercalation Reaction of Calcium from Calcium Disilicide. Synthesis of Layered Polysilane. *Materials Research Bulletin* **1996**, *31*, 307-316.

(52) Chernozatonskii, L. A.; Sorokin, P. B.; Kvashnin, A. G.; Kvashnin, D. G. Diamond-Like C2H Nanolayer, Diamane: Simulation of the Structure and Properties. *Jetp Letters* **2009**, *90*, 134-138.

(53) Chernozatonskii, L. A.; Sorokin, P. B. Nanoengineering Structures on Graphene with Adsorbed Hydrogen "Lines". *Journal of Physical Chemistry C* **2010**, *114*, 3225-3229.

(54) Chernozatonskii, L. A.; Sorokin, P. B.; Kuzubov, A. A.; Sorokin, B. P.; Kvashnin, A. G.; Kvashnin, D. G.; Avramov, P. V.; Yakobson, B. I. Influence of Size Effect on the Electronic and Elastic Properties of Diamond Films with Nanometer Thickness. *Journal of Physical Chemistry C* **2011**, *115*, 132-136.

(55) Chernozatonskii, L. A.; Mavrin, B. N.; Sorokin, P. B. Determination of Ultrathin Diamond Films by Raman Spectroscopy. *Physica Status Solidi B-Basic Solid State Physics* **2012**, *249*, 1550-1554.

(56) Novoselov, K. S.; Jiang, D.; Schedin, F.; Booth, T. J.; Khotkevich, V. V.; Morozov, S. V.; Geim, A. K. Two-Dimensional Atomic Crystals. *Proceedings of the National Academy of Sciences of the United States of America* **2005**, *102*, 10451-10453.

(57) Sterrer, M.; Risse, T.; Pozzoni, U. M.; Giordano, L.; Heyde, M.; Rust, H. P.; Pacchioni, G.; Freund, H. J. Control of the Charge State of Metal Atoms on Thin MgO Films. *Physical Review Letters* **2007**, *98*, 096107.

(58) Benameur, M. M.; Radisavljevic, B.; Heron, J. S.; Sahoo, S.; Berger, H.; Kis, A. Visibility of Dichalcogenide Nanolayers. *Nanotechnology* **2011**, *22*, 5.

(59) Late, D. J.; Liu, B.; Matte, H.; Rao, C. N. R.; Dravid, V. P. Rapid Characterization of Ultrathin Layers of Chalcogenides on SiO2/Si Substrates. *Advanced Functional Materials* **2012**, *22*, 1894-1905.

(60) Blake, P.; Hill, E. W.; Neto, A. H. C.; Novoselov, K. S.; Jiang, D.; Yang, R.; Booth, T. J.; Geim, A. K. Making Graphene Visible. *Applied Physics Letters* **2007**, *91*, 063124.

(61) Magonov, S. N.; Whangbo, M.-H. *Surface Analysis with STM and AFM: Experimental and Theoretical Aspects of Image Analysis*; VCH: Weinheim; New York; Basel; Cambridge; Tokyo, 1996.

(62) *Surface Analysis: The Principal Techniques*; 2nd ed.; Vickerman, J. C.; Gilmore, I. S., Eds.; Wiley: West Sussex, 2009.

(63) Bermejo, D.; Cardona, M. Infrared-Absorption in Hydrogenated Amorphous and Crystallized Germanium. *Journal of Non-Crystalline Solids* **1979**, *32*, 421-430.

(64) Cardona, M. Vibrational-Spectra of Hydrogen in Silicon and Germanium. *Physica Status Solidi B-Basic Research* **1983**, *118*, 463-481.

(65) Jorgense.Ck; Berthou, H. Relative Intensities and Widths of X-Ray Induced Photoelectron Signals from Different Shells in 72 Elements. *Faraday Discussions* **1972**, *54*, 269-276.

(66) Berthou, H.; Jorgensen, C. K. Relative Photoelectron Signal Intensities Obtained with a Magnesium X-Ray Source. *Analytical Chemistry* **1975**, *47*, 482-488.

(67) Castle, J. E.; West, R. H. Bremsstrahlung-Induced Auger Peaks. *Journal of Electron Spectroscopy and Related Phenomena* **1980**, *18*, 355-358.

(68) Szajman, J.; Jenkin, J. G.; Leckey, R. C. G.; Liesegang, J. Subshell Photo-Ionization Cross-Sections, Electron Mean Free Paths and Quantitative X-Ray Photoelectron-Spectroscopy. *Journal of Electron Spectroscopy and Related Phenomena* **1980**, *19*, 393-408.

(69) Yabe, K.; Yamashina, T. Experimental-Determination of Relative Sensitivity in X-Ray Photo-Electron Spectroscopy. *Applied Surface Science* **1981**, *8*, 387-396.

(70) Wagner, C. D.; Davis, L. E.; Zeller, M. V.; Taylor, J. A.; Raymond, R. H.; Gale, L. H. Empirical Atomic Sensitivity Factors for Quantitative-Analysis by Electron-Spectroscopy for Chemical-Analysis. *Surface and Interface Analysis* **1981**, *3*, 211-225.

(71) Nefedov, V. I.; Sergushin, N. P.; Salyn, Y. V.; Band, I. M.; Trzhaskovskaya, M. B. Relative Intensities in X-Ray Photoelectron-Spectra .2. *Journal of Electron Spectroscopy and Related Phenomena* **1975**, *7*, 175-185.